

The Third Dimension of Ferroelectric Domain Walls

Erik D. Roede, Konstantin Shapovalov, Thomas J. Moran, Aleksander B. Mosberg, Zewu Yan, Edith Bourret, Andres Cano, Bryan D. Huey, Antonius T. J. van Helvoort, and Dennis Meier*

Ferroelectric domain walls are quasi-2D systems that show great promise for the development of nonvolatile memory, memristor technology, and electronic components with ultrasmall feature size. Electric fields, for example, can change the domain wall orientation relative to the spontaneous polarization and switch between resistive and conductive states, controlling the electrical current. Being embedded in a 3D material, however, the domain walls are not perfectly flat and can form networks, which leads to complex physical structures. In this work, the importance of the nanoscale structure for the emergent transport properties is demonstrated, studying electronic conduction in the 3D network of neutral and charged domain walls in ErMnO_3 . By combining tomographic microscopy techniques and finite element modeling, the contribution of domain walls within the bulk is clarified and the significance of curvature effects for the local conduction is shown down to the nanoscale. The findings provide insights into the propagation of electrical currents in domain wall networks, reveal additional degrees of freedom for their control, and provide quantitative guidelines for the design of domain-wall-based technology.

corrugation phenomena and curvature effects can contribute to the stability and give rise to anisotropic, as well as enhanced mechanical, optical, and electronics responses. Fascinating examples are Hall effects in bilayer graphene,^[1] and crystals of artificial atoms forming in MoS_2 ,^[2] which indicate strong correlations between electrical conduction and deviations from a perfectly flat structure. Recently, ferroelectric domain walls emerged as a completely new type of 2D system with a particularly strong correlation between morphology and electrical responses.^[3–6] The domain walls exhibit a finite thickness on the order of 1–10 Å, because of which they are often referred to as quasi-2D system. Aside from their finite thickness, and analogous to corrugated 2D materials, the walls are not strictly 2D in the sense that they do not develop a perfectly flat structure. Bending and curvature naturally occur to minimize

1. Introduction

Geometric corrugation effects play an important role in the physical properties of 2D materials. In systems such as single-layer graphene and transition-metal dichalcogenides, geometric

electrostatic stray fields, ensure mechanical compatibility, or due to point defects that lead to domain wall roughening.^[7–10] Importantly, any change in orientation with respect to the electric polarization of the host material directly leads to a modification of the charge state and, hence, the local carrier

E. D. Roede, D. Meier
Department of Materials Science and Engineering
NTNU Norwegian University of Science and Technology
Trondheim 7491, Norway
E-mail: dennis.meier@ntnu.no

K. Shapovalov
Institut de Ciència de Materials de Barcelona (ICMAB-CSIC)
Campus UAB
Bellaterra 08193, Spain

T. J. Moran, B. D. Huey
Department of Materials Science and Engineering
University of Connecticut
Storrs, CT 06269, USA


A. B. Mosberg, A. T. J. van Helvoort
Department of Physics
NTNU Norwegian University of Science and Technology
Trondheim 7491, Norway

A. B. Mosberg
SuperSTEM
STFC Daresbury Laboratories
Keckwick Lane, Warrington WA4 4AD, UK

Z. Yan
Department of Physics
ETH Zurich
Zürich 8093, Switzerland

Z. Yan, E. Bourret
Materials Sciences Division
Lawrence Berkeley National Laboratory
Berkeley, CA 94720, USA

A. Cano
Université Grenoble Alpes, CNRS, Grenoble INP
Institut Néel
Grenoble, France

 The ORCID identification number(s) for the author(s) of this article can be found under <https://doi.org/10.1002/adma.202202614>.

© 2022 The Authors. Advanced Materials published by Wiley-VCH GmbH. This is an open access article under the terms of the Creative Commons Attribution License, which permits use, distribution and reproduction in any medium, provided the original work is properly cited.

DOI: 10.1002/adma.202202614

concentration and conductivity.^[11,12] This one-to-one correlation between the domain wall orientation and its electronic properties, combined with the spatial mobility of the walls, gives rise to unique functionalities that inspired the emergent field of domain wall nanoelectronics.^[13–15]

In contrast to suspended monolayers, the ferroelectric domain walls are internal 2D systems arising within the bulk, where they separate domains with different orientation of the electric polarization P . Thus, their intrinsic electronic transport properties are difficult to access. The conduction of ferroelectric domain walls at surfaces and in near-surface regions has been analyzed by different scanning probe,^[16–19] and electron microscopy techniques,^[20–25] and the 3D behavior has been concluded from scans obtained on different surfaces. To resolve the currents that go through individual ferroelectric domain walls, top and bottom electrodes have been applied to thin films,^[16,26,27] single-crystals,^[12,28,29] and focused ion beam (FIB)-cut lamellas.^[30] Such two-terminal measurements have also been combined with domain imaging on the contacted surfaces to correlate the transport behavior with the domain wall orientation relative to P , but without resolving the sub-surface structure ($P = |\mathbf{P}|$).

Determining the 3D domain wall structure is crucial to gain quantitative information and understand the complex nanoscale physics as reflected, for example, by the investigations on $\text{Pb}(\text{Zr}_{0.2}\text{Ti}_{0.8})\text{O}_3$ (PZT). PZT thin films with out-of-plane P exhibit enhanced conductance at their nominally neutral 180° domain walls, which has been proposed to arise from local head-to-head sections (positively charged) within the material.^[20,27,31] Similarly, the metallic conductance at the nominally neutral domain walls of nanodomains in PZT has been attributed to pronounced curvature effects, leading to strongly charged wall segments below the surface.^[32] Another more recent example is the observation of conductance modulations at nominally neutral domain walls in ErMnO_3 ,^[19] which have been argued to arise as the walls within the material bend away from the charge-neutral position.

To fill this gap in characterization and correlate the electronic conduction along ferroelectric domain walls to their 3D physical structure, different microscopy-based approaches have been explored. The general strategy is to combine two complementary imaging techniques using one to determine the domain wall orientation and a second to measure the local conductance. For example, domain imaging on opposite surfaces by piezoresponse force microscopy (PFM),^[29] and scanning electron microscopy (SEM),^[30] has been applied to LiNbO_3 and ErMnO_3 , respectively, to estimate inclination angles α between the domain wall normal \mathbf{n} and the direction of \mathbf{P} ($\alpha = \angle(\mathbf{P}, \mathbf{n})$). Based on the data, the average density of domain wall bound charges was calculated ($\rho = 2|\mathbf{P}|\cos\alpha$) and compared with local transport data gained by conductive atomic force microscopy (cAFM). Such measurements were successful in demonstrating the predicted correlation between emergent domain wall currents and ρ ,^[11,33] but disregarded the nanoscale structure of the walls,^[34–36] prohibiting a quantitative analysis at the relevant length scale. Although higher resolution of the domain wall orientation can be achieved by performing transmission electron microscopy,^[37] or by correlating PFM and cAFM scans on domain walls in cross-sectional geometry,^[38] these approaches

remain 2D without resolving the wall propagation in the third dimension. This limitation has been overcome by applying optical microscopy, measuring the 3D domain wall structure in LiNbO_3 ^[39–42] and LiTaO_3 ^[43,44] by Cherenkov and nonlinear second-harmonic generation, respectively. Although these measurements represent an important breakthrough regarding the 3D characterization of ferroelectric domain walls, their application is restricted to ferroelectrics with specific optical responses. Furthermore, the resolution limit (currently $\approx 1 \mu\text{m}$) has to be pushed to the nanoscale to access the local variations in orientation that determine the charge state, and complementary transport measurements remain vital to characterize the electronic domain wall properties.

Here, we combine FIB, SEM, and scanning probe microscopy (SPM) to resolve the 3D domain wall structure in ferroelectric ErMnO_3 and simultaneously record the transport properties with nanoscale spatial precision. The FIB-SEM tomography data correlate the electronic conduction to the local orientation of the domain walls within a single experiment and facilitate realistic calculations that reveal how injected currents spread within the 3D domain wall network. Effects from curvature are studied by high-resolution topographic atomic force microscopy (AFM) and finite-elements calculations, quantifying the additional variations in electronic conduction that arise whenever the domain wall structure deviates from a perfectly flat plane-like geometry.

2. FIB-SEM Tomography for Correlated Structure and Conduction Determination in 3D

For our study, we use the uniaxial ferroelectric ErMnO_3 ,^[45] ($T_C = 1470 \text{ K}$) with a saturation polarization $P_S \approx 6 \mu\text{C cm}^{-2}$ oriented along the c -axis of the hexagonal unit cell (see Experimental Section for details).^[46,47] The material develops a 3D network of meandering domain walls, containing topologically protected vortex structures between which the walls continuously change their charge state as seen in **Figure 1a**.^[12,48] It is established that wherever the domain walls come to the surface, their electronic transport properties are dominated by the domain-wall-bound charges.^[12] The latter gives rise to sections that behave as insulating (positively charged, head-to-head), bulk-like (neutral, side-by-side), and conducting (negatively charged, tail-to-tail) as reflected by the correlated cAFM and SEM data in **Figure 1a,b**.^[12,48,49] Although the basic nanoscale physics of the domain walls is well understood, it remains unclear how the injected currents propagate through the 3D domain wall network within the bulk and to what extent the hidden sub-surface structures determine the measured electronic responses. Thus, ErMnO_3 represents an ideal model system for studying the impact of the 3D nanoscale structure and emergent corrugation phenomena on the transport properties at ferroelectric domain walls.

In order to resolve both the 3D domain wall morphology and the local electronic conduction, we combine SEM imaging and FIB tomography, cutting sequential cross-sections into an ErMnO_3 single crystal with out-of-plane P . This procedure leads to the image stack presented in **Figure 1c**, where x , y , and z represent the laboratory coordinate system such that the imaged

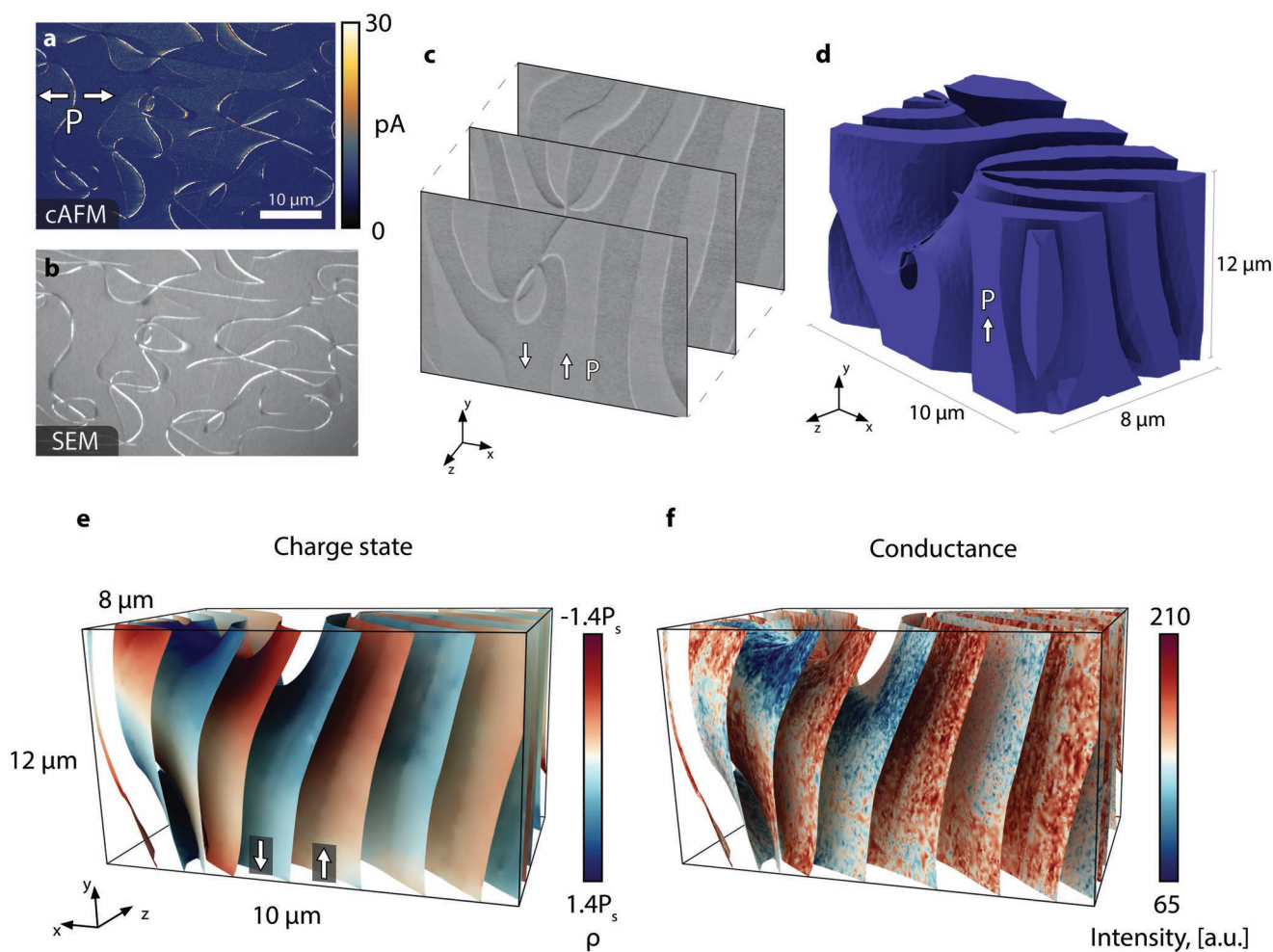


Figure 1. Domain wall charge state and electronic transport properties in 3D. a) cAFM scan showing conducting and insulating domain walls in ErMnO_3 acquired on a (110)-oriented surface with in-plane polarization ($P||c$). The arrows indicate the polarization direction of the 180° domains. b) SEM image gained at the same position as the cAFM scan in (a), showing a one-to-one correlation between the cAFM and SEM contrasts. c) Selected SEM images from the FIB tomography experiment, obtained during the process of cutting 25 nm z-slices by FIB. In addition to the domain walls, the SEM data show domain contrast, indicating a non-zero out-of-plane polarization component for the slices shown. d) 3D rendering visualizing the 3D domain structure resolved by FIB tomography. Domains with polarization pointing down ($-P$) are rendered transparent. e) Domain wall orientation and charge state extracted from the volume in (d). The different colors indicate the domain wall bound charge (blue: positively charged, red: negatively charged) of the domain walls at each point as calculated by projecting the surface normal, \mathbf{n} , of the wall onto the polarization direction. For reference, the density of bound charges at fully charged walls is $2P_s$. f) The same domain walls as in (e), colored according to the measured SEM intensity; red and blue represent high and low conductivity, respectively.

cross-sections are in the xy plane, with polarization oriented in-plane. Consistent with previous SEM surface studies,^[50] domains with opposite polarization orientation are visible as bright ($+P$) and dark ($-P$) regions. In addition, throughout the image series, we observe pronounced domain wall contrast, which correlates with their transport properties as reported in ref. [29] and demonstrated in Figure 1a,b. For the applied imaging conditions (Experimental Section), the conducting tail-to-tail domain walls are brighter than the ferroelectric domains, whereas the insulating head-to-head domain walls are darker, representing a measure for the local electronic conductance. Such SEM conductivity contrast^[25,30] arises at the tail-to-tail domain walls as their enhanced conductivity suppresses surface charging under the electron beam. Vice versa, surface charging is enhanced at the insulating head-to-head domain

walls, leading to a higher surface potential than in the domains. Because of the positive charging at head-to-head domain walls, the landing energy of primary electrons is higher, which gives a lower secondary electron emission yield (dark contrast) in our SEM experiment. Negative charging at the tail-to-tail walls has the opposite effect, so that they exhibit bright contrast. We note, however, that the SEM contrast depends on the imaging conditions. Thus, to clarify the underlying mechanism and establish the relation between emergent SEM contrasts and local conductance, correlated transport measurements as shown in Figure 1a,b are crucial. In total, a volume of $13.8 \times 9.2 \times 10.9 \mu\text{m}^3$ is imaged with 437 slices and a pitch of 25 nm. The intensity voxel matrix from the tomography data is then reconstructed as explained in Experimental Section, which allows for generating a 3D mesh and selectively visualizing the

full 3D domain and domain wall structures as presented in Figure 1d–f. Figure 1d presents a 3D view of the domain distribution in ErMnO_3 . The $+P$ domains are colored purple and $-P$ domains are rendered invisible, revealing the curvature of the different domain walls in sub-surface regions and the presence of otherwise hidden vortex–anti-vortex pairs where the domain walls meet as explained elsewhere.^[48]

Based on the 3D data, the charge state at every point on the domain wall network is calculated. For this purpose, the local domain wall normal, \mathbf{n} , is projected onto the direction of \mathbf{P} , which leads to the map of domain wall bound charges in Figure 1e (positively charged: blue; negatively charged: red). This tomography-based procedure for evaluating the domain wall charge state is analogous to earlier optical approaches,^[41,42] but the application of SEM imaging substantially enhances the spatial resolution, providing a much more accurate picture of the 3D morphology and electrostatic potential landscape at the nanoscale.

Most importantly, as the SEM intensity is determined by the domain wall conductance (Figure 1a,b),^[30] the transport properties are mapped simultaneously along with the domain wall orientation. The respective 3D conductance map is presented in Figure 1f, with high (red) and low (blue) SEM intensity indicating enhanced and reduced electronic conduction, respectively, compared to the domains. The comparison of the data in Figure 1e,f shows a one-to-one correlation between the 3D representation of \mathbf{n} and the local conductance. This result expands previous transport studies on charged domain walls into the third dimension and highlights the importance of the sub-surface structure which defines the out-of-plane component of \mathbf{n} , co-determining the local conductance.

To gain quantitative insight and understand how the 3D structure of ferroelectric domain walls impacts the response measured in 2D conductance maps, we FIB-cut a micrometer-sized sample out of an ErMnO_3 crystal as displayed in Figure 2a ($V = 10.7 \times 14.8 \times 18.2 \mu\text{m}^3$). In contrast to Figure 1, where the probed volume is surrounded by other domains, this geometry ensures that injected currents propagate through a fully characterized domain wall network. The comparison of the data in Figure 2a with PFM and cAFM scans from the top surface (Figure 2b) shows that the SEM contrast correlates with the domain wall conductance, analogous to the experiments performed on macroscopic samples (Figure 1). The corresponding 3D domain structure resolved by FIB-SEM tomography is presented in Figure 2c (voxels: $10 \times 10 \times 10 \text{ nm}^3$). Our tomography data reveals that several vortex lines and strongly curved domain walls are present within the volume. Furthermore, as the data gives the full 3D domain wall orientation (shown for the surface plane in Figure 2d), geometry-related uncertainties in the cAFM data (Figure 2b) become quantifiable. Figure 2e compares the conduction measured at three tail-to-tail domain walls, indicated by the red line in Figure 2b. Although the walls seemingly exhibit the same local orientation with respect to \mathbf{P} , substantial variations in domain wall conductance are observed ranging from 25% to 150% higher currents than for the domains. This difference clearly demonstrates the impact of the sub-surface orientation and the 3D inclination angle that determines the actual charge state. The latter is given by the data points in Figure 2e, showing the same

trend as the local conductance. Note that the domain walls in this example are rather straight. Deviations in the estimation of ρ will be even more pronounced when considering strongly curved domain walls as observed, for example, close to vortex points in ErMnO_3 (Figure 2),^[36] as well as nanodomains in PZT ^[32] and BiFeO_3 .^[51]

3. Current Injection into 3D Domain Wall Networks

In the next step, we investigate how injected currents spread within the 3D domain wall network to determine the volume fraction that controls the electronic response observed at the surface. For this purpose, we consider the tail-to-tail domain wall highlighted by the red line in Figure 2c and model the spreading of current injected into the structure at the position of the red dot. The conductivity, σ , is modified at domain walls and vortex lines with respect to the domains, being proportional to the local density of mobile carriers. The latter is approximated as $\sigma = \sigma_{\text{bulk}} \exp(\nabla \cdot \mathbf{P}/s)$, where s defines the maximum conductivity, which arises at the fully charged tail-to-tail domain walls.^[12,49] Figure 3a presents both the calculated current distribution and the measured charge state of the domain walls in 3D. We find that even for the domain walls with enhanced electronic conduction, a substantial amount of current is flowing through the adjacent domains, consistent with previous analytical solutions for simplified wall geometries.^[12] The relative conductance at domain walls, $G_{\text{DW}}/G_{\text{bulk}}$, is dominated by two dimensionless parameters, that is, the ratio r/ξ between contact radius ($r \approx 4 \text{ nm}$)^[52] and wall width ($\xi \approx 1 \text{ nm}$)^[36] and the ratio between the intrinsic domain wall conductivity and that of the bulk, $\sigma_{\text{DW}}^{\text{max}}/\sigma_{\text{bulk}}$. As measurements of the intrinsic conductivity at ferroelectric domain walls remain an open and particularly challenging task,^[53] the latter is treated as a phenomenological fitting parameter in our model. For $\sigma_{\text{DW}}^{\text{max}}/\sigma_{\text{bulk}} = 150$, a realistic conductance of $G_{\text{DW}} = 7.5G_{\text{bulk}}$ is obtained for a tail-to-tail domain wall oriented perpendicular to the surface, which is in reasonable agreement with local conductance measurements^[12,54] and previous simulations performed for a much smaller r/ξ ratio.^[12] Considering the real domain wall geometry and the injection point marked in Figure 2c, we find $G_{\text{DW}} = 1.4G_{\text{bulk}}$.

Most importantly, Figure 3a shows that the injected current flows through more than one wall, representing a superposition of different walls with continuously varying charge states. In hexagonal manganites, additional complication potentially arises from the presence of topologically protected vortices as seen in the center of Figure 3a (highlighted by the dashed circle), which can act as current dividers within the domain wall network. Because of the complexity of the current distribution in Figure 3a, it is clear that local transport measurements gained at the surface yield only a very rough estimate. This is a general problem for the research on domain walls, hampering the development of more precise models that allow for disentangling the different emergent conduction contributions.^[53,55] However, Figure 3a also reveals that the current density quickly drops off with increasing distance from the surface. For the ideal case of a completely homogeneous material, the electric

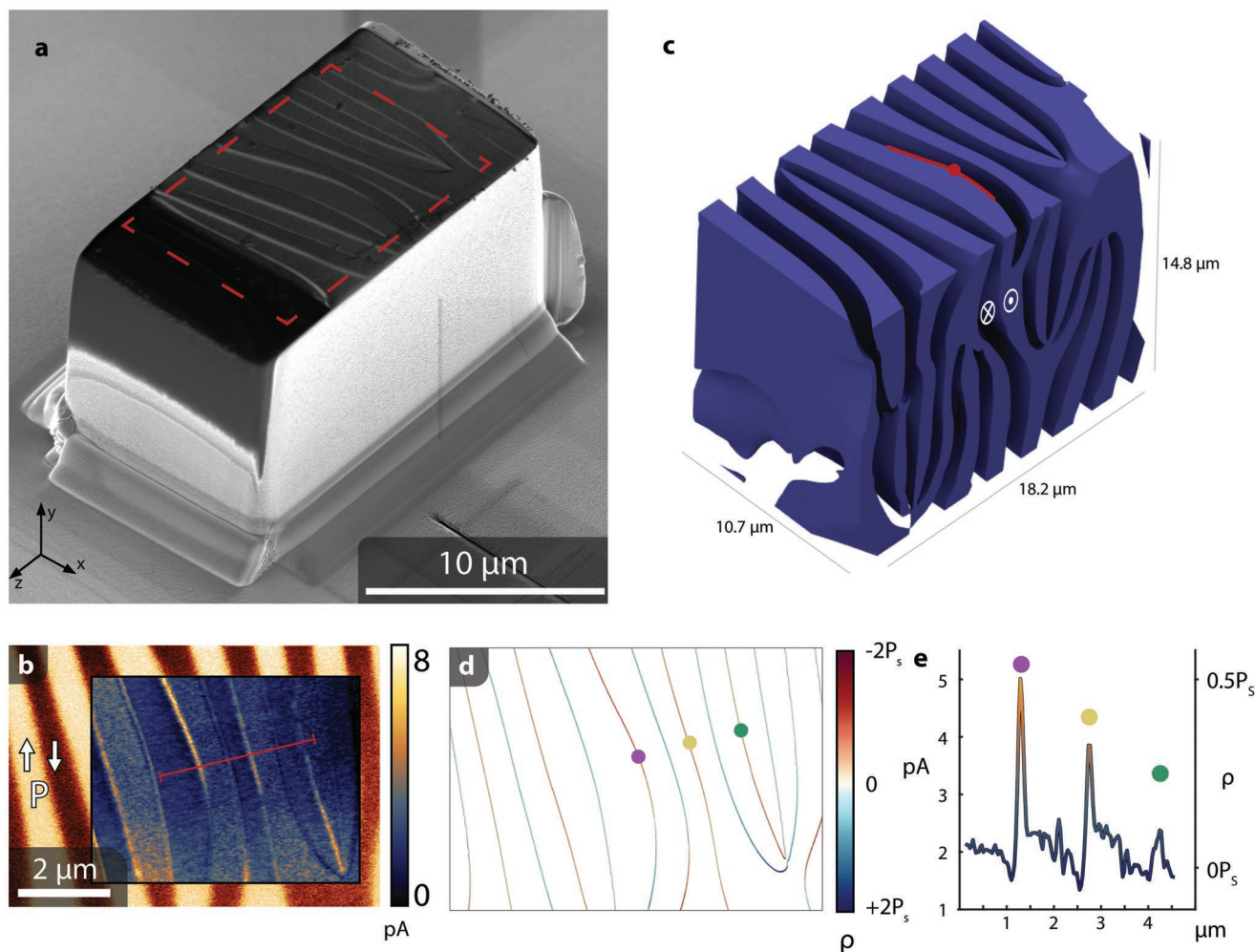


Figure 2. Correlation between domain wall conductivity and 3D inclination angle. a) Sample prepared by FIB liftout, attached to a conductive substrate with top surface polished using 5 kV Ga^+ ions. b) PFM (in-plane contrast) scan from the region marked by the dashed line in (a), showing ferroelectric domains with polarization directions marked by white arrows. Inset: cAFM scan obtained at 10 V showing conductive domain walls. c) Reconstructed volume from FIB tomography of the sample shown in (a) with one polarization domain rendered transparent and polarization directions marked by the white symbols (the red line and dot mark the domain wall and point of current injection investigated in the simulations in Figure 3). d) Slice from the top of the volume shown in (c) corresponding to the surface imaged in (b), colored according to the 3D charge state (as shown in Figure 1e). The colored dots correspond to the wall positions measured in (b). e) Line plot showing current cross-section from a cAFM scan along the red line in (b) over three conductive domain walls (averaged over 10 pixels width). The three walls have the same local orientation at the surface, but exhibit different conductance. The colored dots show the real charge state as determined from the 3D geometry in (c), confirming that the domain walls in fact have different charge densities.

potential can be estimated to drop by 75% over a distance $d \approx 8$ nm for a tip–surface contact radius of $r \approx 4$ nm.^[56,57]

To gain a realistic estimate for the domain walls in ErMnO_3 , we consider a tail-to-tail domain wall modeled as a conducting 2D channel with varying penetration depths as illustrated in the inset of Figure 3b. The calculated conductance G_{DW} is then a function of the cut-off length, L , normalized to the conductance of the bulk G_{bulk} . The result demonstrates that for a fully charged tail-to-tail wall, 90% of the conductance signal originates from a depth of $\lesssim 50$ nm. As the conductance in Figure 3b plateaus at ≈ 50 nm ($= L_c$), the domain wall geometry and emergent vortex lines further away from the surface are practically irrelevant and the sample essentially behaves like an ohmic resistor. We note that, in general, L_c quickly decreases

as domain walls tilt away from the fully charged tail-to-tail state; for a partially charged tail-to-tail domain wall inclined by 45° with respect to \mathbf{P} ($\sigma_{\text{DW}}/\sigma_{\text{bulk}} = 12$), we find $L_c \approx 15$ nm (see Figure S2, Supporting Information). Vice versa, in systems with higher domain wall conductivities, substantially larger L_c values are expected, scaling as $L_c \propto \sigma_{\text{DW}}^{0.7}$ (see Note S2, Supporting Information). Thus, for materials such as LiNbO_3 , where the domain wall conductivity can be more than 14 orders of magnitude higher than in the bulk, L_c reaches the micrometer range.^[58]

In summary, Figure 3 demonstrates the existence of a domain-wall-specific cut-off length, L_c , which is determined by the relative conductance $G_{\text{DW}}/G_{\text{bulk}}$. Within this cut-off length, the domain wall charge state and connections with other

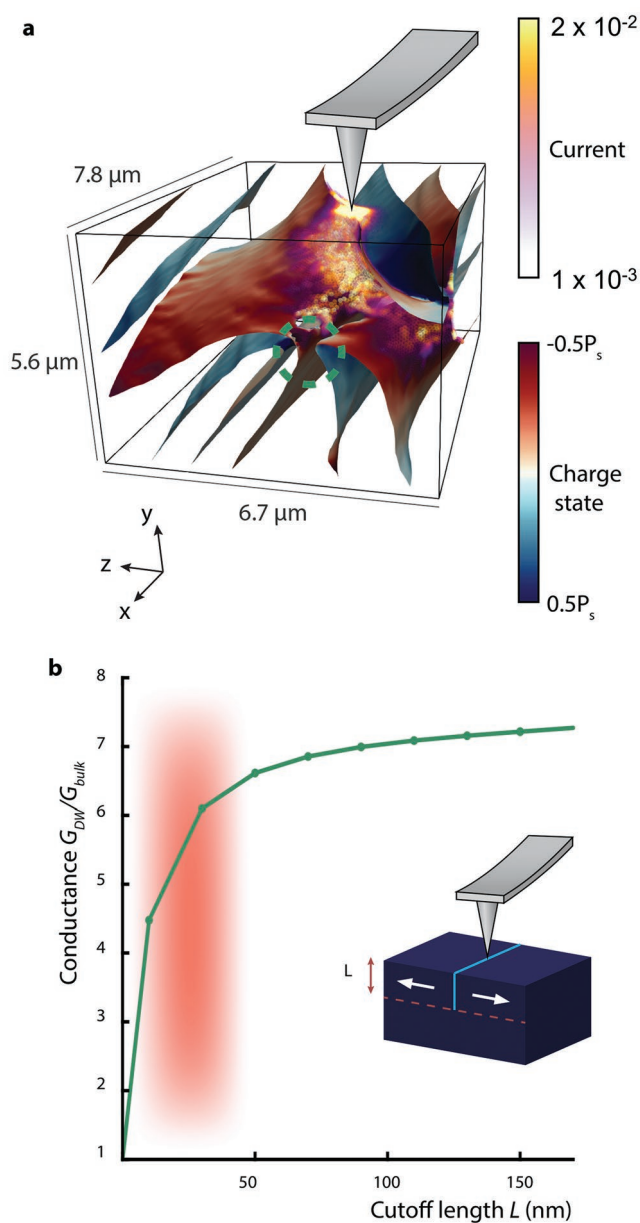


Figure 3. Current spreading in a 3D domain wall network. a) Calculated distribution of electrical current injected into the domain wall network in Figure 2c at the position marked by the red dot. The current spreads over different walls with the vortex (green dashed circle) acting as current divider. b) Calculated normalized conductance as a function of the cut-off length, L . The cut-off length is defined as illustrated in the inset, representing a measure for the domain wall segment that dominates the conduction properties. The data shows that 90% of the measured conductance originate from a depth of ≤ 50 nm.

domain walls are critical, controlling the current path and, hence, the measured domain wall conductivity. This observation highlights the importance of the near-surface domain wall nanostructure beyond just the 3D inclination angle, including corrugation phenomena and curvature effects promoted by, for example, the surface termination, local electrostatics, and strain. Furthermore, it suggests an additional and even stronger

mechanism for controlling the transport properties at domain walls, leveraging permanent or transient changes in curvature rather than by varying the domain wall position or overall tilt angle.

4. Relation Between Domain Wall Curvature and Electronic Transport

To explore and quantify the nanoscale curvature-driven conduction contributions that arise in ErMnO_3 , we resolve the near-surface domain wall nanostructure using a PFM version of high-resolution tomographic AFM^[59] and calculate resulting variations in conductivity. Tomographic PFM facilitates ultra-high volumetric resolution of domains,^[60,61] in this case implementing voxels of $15.6 \times 15.6 \times 5 \text{ nm}^3$, making it an ideal tool for determining near-surface domain wall tilts and curvature. Figure 4a presents a 3D tomogram of all domain walls within an $8 \times 4 \times 0.2 \mu\text{m}^3$ block of excavated material from the same batch as investigated in Figures 1–3. Based on the data, substantial and heterogeneous nanoscale curvature is confirmed not just at the surface but also into the depth.

Figure 4b demonstrates three representative cross-sections extracted from the original piezoresponse tomogram. Overlays of the domain wall location into the depth are also shown, along with a 100 nm radius of curvature circle to guide the eye. Figure 4c presents a histogram of such curvatures calculated for a total of 231 points from three cross-sections. There are many regions which locally exhibit curvatures less than 100 nm, a broader peak around 150 nm, and visually there are many sections without extensive curvature along the z -axis. If such various domain wall structures can be engineered or even temporally controlled, then their influence on the conductance could be profound according to Figure 4d. This plot reveals the range of conductances achievable for tail-to-tail domain walls that are either tilted or curved as defined in the inset. Specifically, variations in the electronic transport are evaluated (see Note S1, Supporting Information) assuming a current is injected into three differently shaped tail-to-tail walls (convex, concave, and tilted straight wall) which symmetrically traverse the same point at a depth of 50 nm. Beyond this point, all walls are assumed to continue as straight walls. This setting allows us to quantify the impact of the curvature for domain walls that nominally exhibit the same average inclination angle, here 60° , focusing on the near-surface region which dominates the measured conductance ($>90\%$ for $L_c = 50$ nm, Figure 3b). The simulation reveals two important effects: First, the curvature of the wall plays a key role in its conductance (see also Figure S3, Supporting Information), leading to substantially different values than calculated from the 3D inclination angle at the surface (see Figure 2e) or the inclination angle averaged over the investigated near-surface layer. For example, for a moderately curved concave tail-to-tail wall ($r = 100$ nm), the extracted conductance is 15% lower than for a straight wall with the same 3D inclination angle at the surface (77° for the dashed blue line) and 18% higher than the green straight wall that goes through the same point at 50 nm depth (solid green line). Second, the direction of curvature has a pronounced influence on the domain wall conductance. For curvature radii similar to those resolved

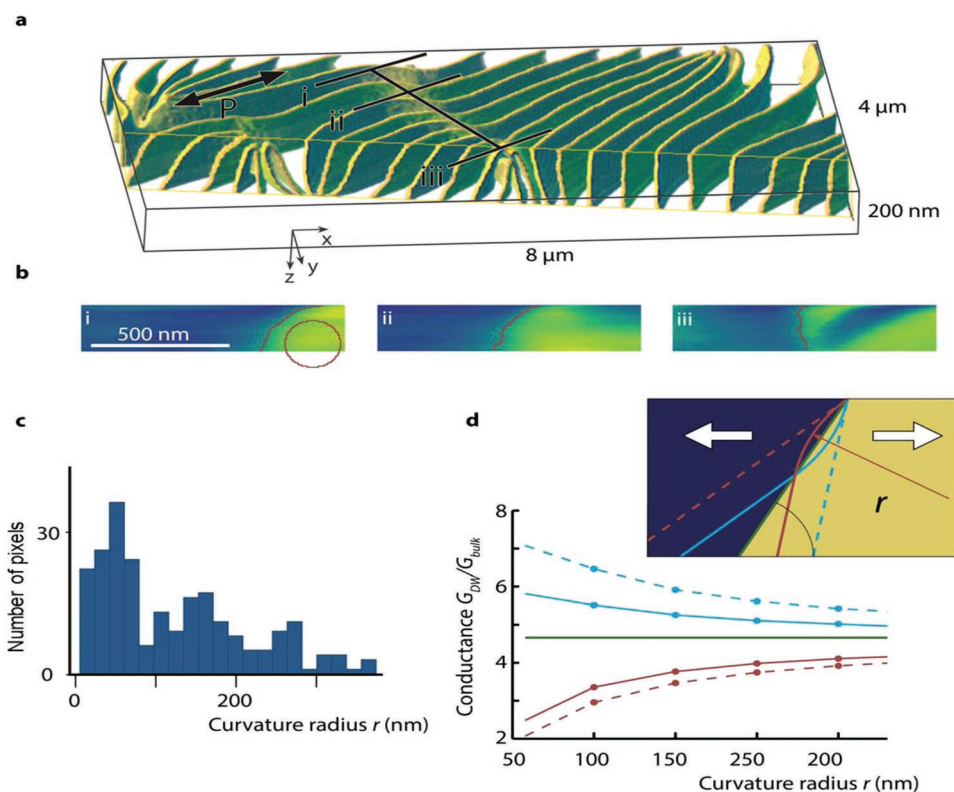


Figure 4. Relation between domain wall curvature and conductance. a) Tomographic PFM data revealing the 3D structure of ferroelectric domain walls in the near-surface region. The black lines indicate the three positions corresponding to the cross-sectional images shown in (b). b) Cross-sectional images revealing the local curvature of three representative domain walls labeled (i) to (iii). A circle of radius 100 nm is shown in (i) to illustrate the respective curvature for reference. c) Domain wall curvature evaluated pixel by pixel for the three domain walls in (b). For the 231 pixels at the walls (marked red in (b)), the curvature radius is calculated and sub-divided into 20 bins. The resulting histogram shows that emergent radii are on the 100 nm length scale. d) Relation between domain wall curvature and conductance. The simulated domain wall geometries are shown in the inset: a planar tail-to-tail domain wall with 60° inclination angle relative to the surface (green), convex/concave curved walls (red/blue) with the same average angle near the surface as the green wall, and straight walls tangent to the curved walls at the surface (dashed red/blue).

by the domain wall tomogram of Figure 4a,b, our model indicates a 60% higher conductance at concave tail-to-tail walls compared to convex ones ($r = 100$ nm). Additional calculations showing how the domain wall conductance changes as function of curvature and the inclination angle at the surface are presented in Figure S3c,d, Supporting Information, respectively, revealing that both parameters are equally important for the transport behavior. The results provide quantitative insight into curvature-driven conduction phenomena, reveal corrugation as an important parameter for controlling the electronic response at ferroelectric domain walls, and suggest a new approach for the design and optimization of domain-wall-based devices.

5. Conclusion

The 3D investigations in this work demonstrate the as-yet-unused nonplanar nature of ferroelectric domain walls as important parameter for controlling the local transport behavior. By leveraging either permanent or temporary variations in curvature, the domain wall resistance can readily be

controlled without the need to completely change the domain wall position or its overall tilt angle. This possibility gives a new dimension to domain wall engineering, enabling the design of two-terminal devices, where continuous variations in conductance could be achieved via static or dynamical curvature effects. Our investigations give detailed information concerning emergent curvature-driven transport phenomena and outline basic criteria for device design, including a practical upper limit for electrode–electrode distances as defined by the cut-off length L_c . In general, depending on the domain wall conductivity, the cut-off length can vary from a few nanometers up to the micrometer range, which implies that the entire domain wall network becomes relevant for the electronic transport behavior in systems with highly conducting walls. The opportunity to generate continuous conductivity changes via curvature effects allows for multi-level resistance control and complex electronic responses based on individual domain walls. With this, we expand the field of domain wall electronics into the realm of nanoscale synaptic devices and unconventional computing, utilizing single ferroelectric domain walls as ultrasmall units that facilitate the desired discrete and tunable functionalities.

6. Experimental Section

Samples: High-quality single crystals of ErMnO_3 were prepared by the pressurized floating-zone method,^[45] oriented by Laue diffraction and cut to disks of about 1 mm thickness. The surfaces were chemomechanically polished using a Logitech PM5 polishing machine with silica slurry. The polished surfaces had a root-mean-square roughness of approximately 1 nm.

FIB-SEM Tomography and Liftout: A Thermo Scientific Helios G4 UX DualBeam FIB-SEM was used for imaging, tomography, and nanostructuring. SEM images were taken at 2 kV acceleration voltage at 0.1 nA beam current, using an in-lens detector with an immersion objective lens. For FIB liftout, a pentagonal prism was extracted in a plan view configuration using an EasyLift EX NanoManipulator and attached to a TEM half grid. The sample was then trimmed to leave a rectangular prism. The bottom face was polished using 5 kV acceleration voltage before the sample was lifted off the TEM grid and Pt-welded to a gold-coated Si substrate and the top face polished at 5 kV. Before tomography, areas of interest were coated with 2 μm ion beam deposited platinum. The Slice and View 4 software was used for automated serial sectioning. For milling, 30 kV ion beam acceleration voltage and 90 to 260 pA beam current was used.

Tomography Image Processing: FIB-based tomography image stacks were aligned using the software ImageJ,^[62,63] by applying a template matching algorithm to superimpose known fixed points. To account for charging artifacts that may occur during SEM imaging, a median line alignment was implemented, adjusting the brightness of each line to equalize the median of each line. To counter the effect of apparent changes in illumination during the tomography procedure, a pseudo flat-field background subtraction was performed by creating and subtracting an artificial background image for each slice. After semiautomated segmentation into different polarization domains, the extracted voxel matrices were processed in ParaView.^[64] A contouring filter was used to extract the domain walls as a 3D mesh, which was smoothed to reduce staircasing artifacts.

Scanning Probe Microscopy (SPM): cAFM and PFM measurements were performed on an Oxford Instruments Cypher ES AFM. For cAFM, TipsNano DCP10 probes were used with a 10 V bias applied to the back of the sample. For PFM, RMN 25PT300B probes were used in lateral dual AC resonance tracking mode around the contact resonance of 229.45 kHz, with 10 V peak-to-peak AC voltage applied. The polarization directions were calibrated on periodically poled LiNbO_3 .

AFM Tomography: Consecutive lateral PFM images were acquired with an Oxford Instruments Cypher VRS AFM, using doped diamond AFM probes (Appnano DD-ACTA) and a Zurich Instruments MFLI lock-in-amplifier. Tip biases on the order of 2 V, at torsional contact resonant frequencies of $\approx 1\text{--}2$ MHz, provided PFM amplitude and phase images as typified by the six representative phase images out of 41 total in Figure S1a, Supporting Information. From these, the piezoresponse was calculated pixel by pixel throughout the entire volume (Figure S1b, Supporting Information) implemented with Matlab using custom but straightforward code which calculates $\text{amplitude} \cdot \sin(\text{phase})$. To better visualize the domain curvature, all positive (bright) domains are removed in (Figure S1c, Supporting Information) and the tomogram was depicted from three slightly different perspectives, based on -20° , 0° , and 20° rotations around the y -axis (as indicated) and with oblique illumination and shadowing (according to a light source shown at lower right). As with the FIB-based tomography, xy position registry and then 3D domain wall identification were both performed using ImageJ. Slicing across multiple domain walls particularly reveals extensive local curvature of the domain patterns throughout x , y , and z , confirming the profoundly 3D nanoscale nature of the domain structure which was otherwise hidden beneath the surface. These results were typical of more than 10 similarly acquired volumes from this same batch of samples as utilized throughout this work.

Finite Element Modeling: All simulations of the current flow in presence of domain walls were done in 3D using the finite-elements method implemented in COMSOL Multiphysics—see details in Note S1, Supporting Information.

Supporting Information

Supporting Information is available from the Wiley Online Library or from the author.

Acknowledgements

The authors acknowledge NTNU for support through the Enabling Nanotechnologies: Nano program. The Research Council of Norway is acknowledged for the support to the Norwegian Micro- and Nano-Fabrication Facility, NorFab, project number 245963/F50. Z.Y. and E.B. were supported by the U.S. Department of Energy, Office of Science, Basic Energy Sciences, Materials Sciences, and Engineering Division under Contract No. DE-AC02-05-CH11231 within the Quantum Materials program-KC2202. D.M. acknowledges funding from the European Research Council (ERC) under the European Union's Horizon 2020 research and innovation program (Grant Agreement No. 863691) and further thanks NTNU for support through the Onsager Fellowship Program and NTNU Stjerneprogrammet. T.J.M. and B.D.H. are grateful for support from NSF DMR:MRI:1726862 to develop T-AFM. K.S. acknowledges the support of the European Research Council under the European Union's Horizon 2020 research and innovation program (Grant Agreement No. 724529) and Ministerio de Economía, Industria y Competitividad through Grant Nos. MAT2016-77100-C2-2-P and SEV-2015-0496.

Conflict of Interest

The authors declare no conflict of interest.

Author Contributions

E.D.R. recorded the PFM/cAFM data and performed the FIB tomography measurements together with A.B.M. under the supervision of D.M. and A.T.J.v.H. K.S. performed the 3D finite-elements modeling of the current flow with support from AC. T.J.M. and B.D.H. conducted and analyzed tomographic AFM. Z.Y. and E.B. provided the materials. D.M. coordinated the project and wrote the manuscript together with E.D.R. All authors discussed the results and contributed to the final version of the manuscript.

Data Availability Statement

The data that support the findings of this study are available from the corresponding author upon reasonable request.

Keywords

domain walls, ErMnO_3 , ferroelectric materials, quasi-2D systems, tomography

Received: March 21, 2022

Revised: June 13, 2022

Published online: August 5, 2022

[1] S.-C. Ho, C.-H. Chang, Y.-C. Hsieh, S.-T. Lo, B. Huang, T.-H.-Y. Vu, C. Ortix, T.-M. Chen, *Nat. Electron.* **2021**, 4, 116.

[2] H. Li, A. W. Contryman, X. Qian, S. M. Ardakani, Y. Gong, X. Wang, J. M. Weisse, C. H. Lee, J. Zhao, P. M. Ajayan, J. Li, H. C. Manoharan, X. Zheng, *Nat. Commun.* **2015**, 6, 7381.

- [3] E. K. H. Salje, *ChemPhysChem* **2010**, *11*, 940.
- [4] D. Meier, *J. Phys.: Condens. Matter* **2015**, *27*, 463003.
- [5] G. F. Nataf, M. Guennou, J. M. Gregg, D. Meier, J. Hlinka, E. K. H. Salje, J. Kreisel, *Nat. Rev. Phys.* **2020**, *2*, 634.
- [6] P. S. Bednyakov, B. I. Sturman, T. Sluka, A. K. Tagantsev, P. V. Yudin, *npj Comput. Mater.* **2018**, *4*, 65.
- [7] T. J. Yang, V. Gopalan, P. J. Swart, U. Mohideen, *Phys. Rev. Lett.* **1999**, *82*, 4106.
- [8] A. K. Tagantsev, L. E. Cross, J. Fousek, *Domains in Ferroic Crystals and Thin Films*, Springer, New York **2010**.
- [9] P. Paruch, T. Giamarchi, J.-M. Triscone, *Phys. Rev. Lett.* **2005**, *94*, 197601.
- [10] D. R. Småbråten, T. S. Holstad, D. M. Evans, Z. Yan, E. Bourret, D. Meier, S. M. Selbach, *Phys. Rev. Res.* **2020**, *2*, 033159.
- [11] E. A. Eliseev, A. N. Morozovska, G. S. Svechnikov, V. Gopalan, V. Y. Shur, *Phys. Rev. B* **2011**, *83*, 235313.
- [12] D. Meier, J. Seidel, A. Cano, K. Delaney, Y. Kumagai, M. Mostovoy, N. A. Spaldin, R. Ramesh, M. Fiebig, *Nat. Mater.* **2012**, *11*, 284.
- [13] G. Catalan, J. Seidel, R. Ramesh, J. F. Scott, *Rev. Mod. Phys.* **2012**, *84*, 119.
- [14] D. Meier, S. M. Selbach, *Nat. Rev. Mater.* **2021**, *7*, 157.
- [15] D. Meier, J. Seidel, M. Gregg, R. Ramesh, *Domain Walls*, Oxford University Press, Oxford, UK **2020**.
- [16] J. Seidel, L. W. Martin, Q. He, Q. Zhan, Y.-H. Chu, A. Rother, M. E. Hawkrigge, P. Maksymovych, P. Yu, M. Gajek, N. Balke, S. V. Kalinin, S. Gemming, F. Wang, G. Catalan, J. F. Scott, N. A. Spaldin, J. Orenstein, R. Ramesh, *Nat. Mater.* **2009**, *8*, 229.
- [17] E. Soergel, *J. Phys. D: Appl. Phys.* **2011**, *44*, 464003.
- [18] J. G. M. Guy, C. Cochard, P. Aguado-Puente, E. Soergel, R. W. Whatmore, M. Conroy, K. Moore, E. Courtney, A. Harvey, U. Bangert, A. Kumar, R. G. P. McQuaid, J. M. Gregg, *Adv. Mater.* **2021**, *33*, 2008068.
- [19] J. Schultheiß, J. Schaab, D. R. Småbråten, S. H. Skjærø, E. Bourret, Z. Yan, S. M. Selbach, D. Meier, *Appl. Phys. Lett.* **2020**, *116*, 262903.
- [20] C.-L. Jia, S.-B. Mi, K. Urban, I. Vrejoiu, M. Alexe, D. Hesse, *Nat. Mater.* **2007**, *7*, 57.
- [21] A.-S. Pawlik, T. Kämpfe, A. Haußmann, T. Woike, U. Treske, M. Knupfer, B. Büchner, E. Soergel, R. Streubel, A. Koitzsch, L. M. Eng, *Nanoscale* **2017**, *9*, 10933.
- [22] J. Schaab, I. P. Krug, F. Nickel, D. M. Gottlob, H. Doğanay, A. Cano, M. Hentschel, Z. Yan, E. Bourret, C. M. Schneider, R. Ramesh, D. Meier, *Appl. Phys. Lett.* **2014**, *104*, 232904.
- [23] C. Becher, L. Maurel, U. Aschauer, M. Lilienblum, C. Magén, D. Meier, E. Langenberg, M. Trassin, J. Blasco, I. P. Krug, P. A. Algarabel, N. A. Spaldin, J. A. Pardo, M. Fiebig, *Nat. Nanotechnol.* **2015**, *10*, 661.
- [24] G. F. Nataf, P. Grysan, M. Guennou, J. Kreisel, D. Martinotti, C. L. Rountree, C. Mathieu, N. Barrett, *Sci. Rep.* **2016**, *6*, 33098.
- [25] K. A. Hunnestad, E. D. Roede, A. T. J. van Helvoort, D. Meier, *J. Appl. Phys.* **2020**, *128*, 191102.
- [26] S. Farokhipoor, B. Noheda, *Phys. Rev. Lett.* **2011**, *107*, 127601.
- [27] J. Guyonnet, I. Gaponenko, S. Gariglio, P. Paruch, *Adv. Mater.* **2011**, *23*, 5377.
- [28] T. Sluka, A. K. Tagantsev, P. Bednyakov, N. Setter, *Nat. Commun.* **2013**, *4*, 1808.
- [29] M. Schröder, A. Haußmann, A. Thiessen, E. Soergel, T. Woike, L. M. Eng, *Adv. Funct. Mater.* **2012**, *22*, 3936.
- [30] A. B. Mosberg, E. D. Roede, D. M. Evans, T. S. Holstad, E. Bourret, Z. Yan, A. T. J. van Helvoort, D. Meier, *Appl. Phys. Lett.* **2019**, *115*, 122901.
- [31] A. Tselev, P. Yu, Y. Cao, L. R. Dedon, L. W. Martin, S. V. Kalinin, P. Maksymovych, *Nat. Commun.* **2016**, *7*, 11630.
- [32] P. Maksymovych, A. N. Morozovska, P. Yu, E. A. Eliseev, Y.-H. Chu, R. Ramesh, A. P. Baddorf, S. V. Kalinin, *Nano Lett.* **2011**, *12*, 209.
- [33] M. Y. Gureev, A. K. Tagantsev, N. Setter, *Phys. Rev. B* **2011**, *83*, 184104.
- [34] J. Gonnissen, D. Batuk, G. F. Nataf, L. Jones, A. M. Abakumov, S. V. Aert, D. Schryvers, E. K. H. Salje, *Adv. Funct. Mater.* **2016**, *26*, 7599.
- [35] Q. H. Zhang, L. J. Wang, X. K. Wei, R. C. Yu, L. Gu, A. Hirata, M. W. Chen, C. Q. Jin, Y. Yao, Y. G. Wang, X. F. Duan, *Phys. Rev. B* **2012**, *85*, 020102.
- [36] M. E. Holtz, K. Shapovalov, J. A. Mundy, C. S. Chang, Z. Yan, E. Bourret, D. A. Muller, D. Meier, A. Cano, *Nano Lett.* **2017**, *17*, 5883.
- [37] J. P. V. McConville, H. Lu, B. Wang, Y. Tan, C. Cochard, M. Conroy, K. Moore, A. Harvey, U. Bangert, L.-Q. Chen, A. Gruverman, J. M. Gregg, *Adv. Funct. Mater.* **2020**, *30*, 2000109.
- [38] Y. Zhang, H. Lu, X. Yan, X. Cheng, L. Xie, T. Aoki, L. Li, C. Heikes, S. P. Lau, D. G. Schlom, L. Chen, A. Gruverman, X. Pan, *Adv. Mater.* **2019**, *31*, 1902099.
- [39] Y. Uesu, H. Shibata, S. Suzuki, S. Shimada, *Ferroelectrics* **2004**, *304*, 99.
- [40] Y. Sheng, A. Best, H.-J. Butt, W. Krolikowski, A. Arie, K. Koynov, *Opt. Express* **2010**, *18*, 16539.
- [41] T. Kämpfe, P. Reichenbach, M. Schröder, A. Haußmann, L. M. Eng, T. Woike, E. Soergel, *Phys. Rev. B* **2014**, *89*, 035314.
- [42] C. Godau, T. Kämpfe, A. Thiessen, L. M. Eng, A. Haußmann, *ACS Nano* **2017**, *11*, 4816.
- [43] S. Cherifi-Hertel, H. Bulou, R. Hertel, G. Taupier, K. D. Dorkenoo, C. Andreas, J. Guyonnet, I. Gaponenko, K. Gallo, P. Paruch, *Nat. Commun.* **2017**, *8*, 15768.
- [44] Y. Uesu, H. Yokota, S. Kawado, J. Kaneshiro, S. Kurimura, N. Kato, *Appl. Phys. Lett.* **2007**, *91*, 182904.
- [45] Z. Yan, D. Meier, J. Schaab, R. Ramesh, E. Samulon, E. Bourret, *J. Cryst. Growth* **2015**, *409*, 75.
- [46] S. C. Chae, N. Lee, Y. Horibe, M. Tanimura, S. Mori, B. Gao, S. Carr, S.-W. Cheong, *Phys. Rev. Lett.* **2012**, *108*, 167603.
- [47] B. B. V. Aken, T. T. M. Palstra, A. Filippetti, N. A. Spaldin, *Nat. Mater.* **2004**, *3*, 164.
- [48] T. Choi, Y. Horibe, H. T. Yi, Y. J. Choi, W. Wu, S.-W. Cheong, *Nat. Mater.* **2010**, *9*, 253.
- [49] W. Wu, Y. Horibe, N. Lee, S.-W. Cheong, J. R. Guest, *Phys. Rev. Lett.* **2012**, *108*, 077203.
- [50] E. D. Roede, A. B. Mosberg, D. M. Evans, E. Bourret, Z. Yan, A. T. J. van Helvoort, D. Meier, *APL Mater.* **2021**, *9*, 021105.
- [51] R. K. Vasudevan, A. N. Morozovska, E. A. Eliseev, J. Britson, J.-C. Yang, Y.-H. Chu, P. Maksymovych, L. Q. Chen, V. Nagarajan, S. V. Kalinin, *Nano Lett.* **2012**, *12*, 5524.
- [52] A. Abdollahi, N. Domingo, I. Arias, G. Catalan, *Nat. Commun.* **2019**, *10*, 1266.
- [53] J. M. Gregg, *Appl. Phys. Lett.* **2022**, *120*, 010501.
- [54] J. Schaab, A. Cano, M. Lilienblum, Z. Yan, E. Bourret, R. Ramesh, M. Fiebig, D. Meier, *Adv. Electron. Mater.* **2015**, *2*, 1500195.
- [55] J. Schultheiß, T. Rojac, D. Meier, *Adv. Electron. Mater.* **2021**, *8*, 2100996.
- [56] F. Llewellyn-Jones, *The Physics of Electrical Contacts*, Clarendon Press, Oxford, UK **1957**.
- [57] R. Holm, *Electric Contacts Handbook*, Springer, Berlin **1958**.
- [58] C. S. Werner, S. J. Herr, K. Buse, B. Sturman, E. Soergel, C. Razzaghi, I. Breunig, *Sci. Rep.* **2017**, *7*, 9862.
- [59] J. Song, Y. Zhou, B. D. Huey, *Appl. Phys. Lett.* **2021**, *118*, 080501.
- [60] J. Song, S. Zhuang, M. Martin, L. A. Ortiz-Flores, B. Paudel, D. Yarotski, J. Hu, A. Chen, B. D. Huey, *Adv. Funct. Mater.* **2021**, *31*, 2102311.
- [61] J. J. Steffes, R. A. Ristau, R. Ramesh, B. D. Huey, *Proc. Natl. Acad. Sci. USA* **2019**, *116*, 2413.
- [62] C. T. Rueden, J. Schindelin, M. C. Hiner, B. E. DeZonia, A. E. Walter, E. T. Arena, K. W. Eliceiri, *BMC Bioinf.* **2017**, *18*, 529.
- [63] J. Schindelin, I. Arganda-Carreras, E. Frise, V. Kaynig, M. Longair, T. Pietzsch, S. Preibisch, C. Rueden, S. Saalfeld, B. Schmid, J.-Y. Tinevez, D. J. White, V. Hartenstein, K. Eliceiri, P. Tomancak, A. Cardona, *Nat. Methods* **2012**, *9*, 676.
- [64] U. Ayachit, *The ParaView Guide : Updated for ParaView Version 4.3*, Kitware, Clifton Park, NY, USA **2015**.